actuators

MDPI

Article

Numerical and Experimental Study of a Wearable Exo-Glove for Telerehabilitation Application Using Shape Memory Alloy Actuators

Mohammad Sadeghi [1,2], Alireza Abbasimoshaei [1,2,*], Jose Pedro Kitajima Borges [1] and Thorsten Alexander Kern [1,2]

[1] Institute for Mechatronics in Mechanics, Hamburg University of Technology (TUHH), Eissendorferstr. 38, 21073 Hamburg, Germany; mohammad.sadeghi@tuhh.de (M.S.); t.a.kern@tuhh.de (T.A.K.)
[2] Haptic Lab, Ligeti Center, Laboratories for Innovation and General-Audience Edification through the Transfer of Ideas, Veritaskai 1, 21079 Hamburg, Germany
* Correspondence: al.abbasimoshaei@tuhh.de

Abstract: Hand paralysis, caused by conditions such as spinal cord injuries, strokes, and arthritis, significantly hinders daily activities. Wearable exo-gloves and telerehabilitation offer effective hand training solutions to aid the recovery process. This study presents the development of lightweight wearable exo-gloves designed for finger telerehabilitation. The prototype uses NiTi shape memory alloy (SMA) actuators to control five fingers. Specialized end effectors target the metacarpophalangeal (MCP), proximal interphalangeal (PIP), and distal interphalangeal (DIP) joints, mimicking human finger tendon actions. A variable structure controller, managed through a web-based Human–Machine Interface (HMI), allows remote adjustments. Thermal behavior, dynamics, and overall performance were modeled in MATLAB Simulink, with experimental validation confirming the model's efficacy. The phase transformation characteristics of NiTi shape memory wire were studied using the Souza–Auricchio model within COMSOL Multiphysics 6.2 software. Comparing the simulation to trial data showed an average error of 2.76°. The range of motion for the MCP, PIP, and DIP joints was 21°, 65°, and 60.3°, respectively. Additionally, a minimum torque of 0.2 Nm at each finger joint was observed, which is sufficient to overcome resistance and meet the torque requirements. Results demonstrate that integrating SMA actuators with telerehabilitation addresses the need for compact and efficient wearable devices, potentially improving patient outcomes through remote therapy.

Keywords: wearable exo-glove; telerehabilitation; shape memory alloy; simulation; human–machine interface

Citation: Sadeghi, M.; Abbasimoshaei, A.; Kitajima Borges, J.P.; Kern, T.A. Numerical and Experimental Study of a Wearable Exo-Glove for Telerehabilitation Application Using Shape Memory Alloy Actuators. *Actuators* **2024**, *13*, 409. https://doi.org/10.3390/act13100409

Academic Editors: Luis Enrique Moreno Lorente, Maria Dolores Blanco Rojas and Dorin Sabin Copaci

Received: 19 August 2024
Revised: 2 October 2024
Accepted: 8 October 2024
Published: 11 October 2024

1. Introduction

Stroke is a major contributor to long-term disability, significantly affecting mobility and overall quality of life. More than 50% of stroke survivors aged 65 and older experience impaired mobility [1]. A World Health Organization (WHO) survey reported that hand dysfunction occurs in over half of these patients [2]. Each year, more than 15 million people globally suffer strokes, with 85% experiencing arm impairment and 40% facing chronic or permanent disabilities [3,4]. Stroke-induced neurological damage impairs muscle control, leading to poor finger coordination and severely impacting daily activities. Hand injuries also significantly contribute to workplace injuries, chronic conditions, lost working hours, and permanent disabilities [5], imposing a considerable burden on families, communities, and nations. Numerous studies have shown that rehabilitation therapy can mitigate stroke complications and promote brain reorganization [6,7]. Rehabilitation focused on hand function, guided by a therapist, is crucial for regaining essential motor skills. However, traditional physical therapy often relies on repetitive tasks, which can be inefficient,

time-consuming, and sometimes impractical. To address these challenges, robotic-assisted technologies have gained significant attention. Researchers have developed robots specifically designed to aid recovery, particularly for hand function [7–14]. These wearable robotic exoskeletons help patients perform hand exercises and various grasping tasks more efficiently [7]. In recent years, the development of wearable devices for rehabilitation has gained significant attention. Various studies have explored the integration of virtual reality (VR) and wearable technology to enhance therapeutic outcomes [8–10]. These systems use the immersive nature of VR to motivate patients, transforming repetitive rehabilitation tasks into interactive and engaging experiences [8]. Bilateral hand training, which uses one glove for sensing and another for actuation, has also been a focus of research [11–13]. This method aims to improve coordination and motor skills by engaging both hands simultaneously, promoting neuroplasticity and functional recovery [11]. Additionally, exoskeleton gloves have been developed to provide controlled and repeatable finger movements, crucial for patients requiring precise and consistent rehabilitation exercises [7]. Most wearable systems rely on a combination of sensing and actuation sources. Sensors such as inertial measurement units (IMUs) [14,15] and force-sensitive resistors (FSRs) [12,16] are commonly used to measure finger movements, providing real-time feedback to enhance the therapeutic process. Flexible FSR sensors are lightweight and inexpensive but only provide the relative position between finger segments and do not offer information on the finger's position in space [16]. In contrast, IMUs are beneficial for rehabilitation gloves because they are compact, lightweight, highly accurate, and able to gather various data, including acceleration and angular velocity, with reasonably low drift [8]. To improve the precision and reliability of exoskeleton robotic gloves, various actuation mechanisms have been studied, including DC motors [12,17–22], linear actuators [23], elastomeric actuators [24], tendon-driven systems [19,25], and pneumatic systems [26–30]. Wearable gloves with pneumatic mechanisms, such as the commercial Haptx Glove [26] or soft fabric-based pneumatic actuators [30], incorporate multiple motors to achieve faithful tactile simulation, allowing for differentiation in sensation based on the contact location on the same fingertip. In another approach, a set of miniature DC or brushless motors [12] actuate the articulated linkages, driving the finger through a cable routing system. Each mechanism presents distinct advantages and disadvantages. For instance, while pneumatic systems are effective, they require substantial resources such as compressors and accumulators, increasing system complexity and volume. In motor-cable systems, as the degrees of freedom and force requirements increase, the system's size and driving power increase accordingly. Consequently, motors may need to be positioned outside the glove, making the system bulky. However, for both driving mechanisms mentioned, the required force range for rehabilitation is reliably achievable [22].

Shape memory alloys (SMAs) are recognized as smart materials capable of reverting to their initial form after deformation when triggered by specific stimuli. This capability arises from a reversible martensitic transformation between the austenite and martensite phases [31]. SMAs are categorized based on the type of stimulus that activates the shape memory effect, such as thermal, magnetic, electrical, or light. Given these unique properties, SMAs have found applications in various engineering fields, including micro-vibratory systems [32], aircraft [33], and tunable dampers [34]. Recently, shape memory wires (SMWs) have gained significant attention for rehabilitation applications [35–37]. For instance, a compact and lightweight wearable glove has been introduced using SMA wires to mimic natural muscle functions [35]. This device effectively controls finger movements through thermal contraction and Pulse Width Modulation (PWM) signals. Another study presents a comfortable haptic glove designed for kinesthetic perception. This glove utilizes SMA springs and flexible stretch sensors to simulate three force levels, providing reasonable haptic feedback for rehabilitation [36]. Additionally, the development and evaluation of a soft exo-glove designed for hemiplegic patients are reported successfully [37]. The exo-glove incorporates knitted SMA actuators, enhancing joint range of motion (ROM) and grip strength through thermal and mechanical stimulation. Despite these advancements, several

challenges remain. Effective heat management, optimizing the balance between functionality and comfort, and ensuring long-term durability are important limitations [35–37]. Moreover, to the author's knowledge, existing SMA wearable gloves lack a usable human–machine interface (HMI) and a system to control finger movements remotely. Addressing these gaps is essential for remote rehabilitation and monitoring patient progress.

In this study, a five-finger telerehabilitation exoskeleton actuated by shape memory alloys was developed. This portable, user-friendly device rehabilitates the metacarpophalangeal (MCP), proximal interphalangeal (PIP), and distal interphalangeal (DIP) joints of the human finger simultaneously, using end effectors that block specific joint motions. As depicted in Figure 1, the flexor and extensor tendons in the human finger are responsible for bidirectional movement. This motion was replicated using a combination of nickel-titanium shape memory wires (SMWs) and springs. A variable structure controller guides the fingers to desired positions and follows a reference path, while a web application provides a human–machine interface for precise control of each finger joint. The thermal behavior of the smart wires and system dynamics were modeled in MATLAB Simulink R2023b. Additionally, the phase change process was studied using the Souza–Auricchio model within the COMSOL 6.2 software package. Both simulation and experimental results confirmed the system's ability to overcome joint resistance, deliver necessary torque, and achieve the required range of motion for effective tele-rehabilitation.

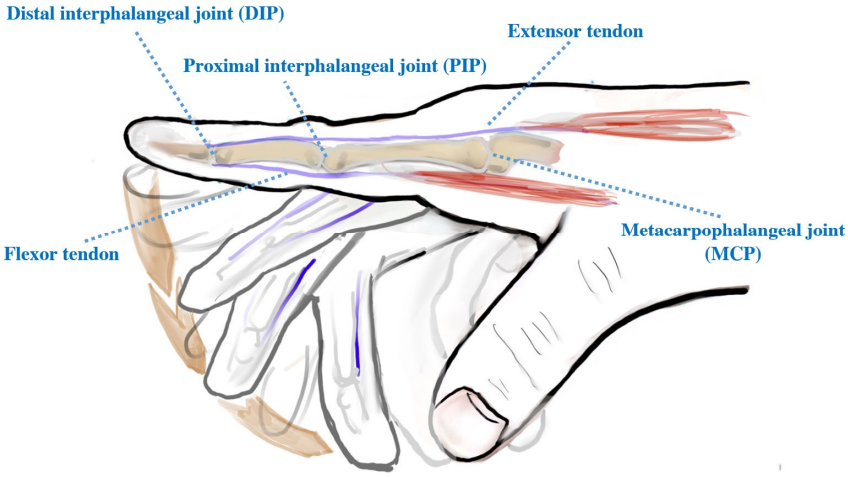

Figure 1. Illustration of the human finger movement mechanism and various joint structures.

2. Materials and Methods

2.1. Experimental Setup

The fabricated exoskeleton glove, including the power system, control module, and end effectors, is illustrated in Figure 2a–e. The exoskeleton comprises three main components: forearm support, hand support, and finger mechanism. The forearm support attaches the system to the user's arm. As shown in Figure 2a, the support features a platform-like structure to accommodate five tuner modules. To ensure ergonomic fitting around the user's arm, Velcro straps are considered for ease of adjustment for different users. At the end of the forearm support, tuner modules were implemented to secure both ends of the SMA wire, maintain their tension, and adjust the initial position of the system.

The SMA wire (375 µm diameter) was arranged in a straight path along the forearm for efficient force transmission. Its initial position and tension were calibrated once during the setup. The knobs of the tuners could be adjusted to achieve the desired tension level and initial position. The SMA wire ends were crimped together with an external wire that provided the stimulation current signal to the SMA wire (55% Ni–45% Ti, Guangdong Metal Corporation, Guangzhou, China). To avoid degradation of the SMA's performance over time beyond the austenite finish (Af) temperature, the stimulation signal was controlled using the Pulse Width Modulation (PWM) technique. The hand support was used to attach the system to the user's arm and had several functions, such as enabling the SMA wire

to pull the input link of the finger mechanism. It also included a slot for a torsion spring to maintain tension and reset the SMA wire. Additionally, a potentiometer, attached by a geared connection, rotated with the input link and allowed for the collection of angular position data for all fingers, which were used in the controller algorithm and during data collection. In designing the finger mechanism, several criteria were considered. The user should be able to close their hand without any components blocking the motion. The necessary range of motion, angular velocity, and torque resistance for rehabilitation purposes were based on a literature review. For the end effectors, which connected the user's fingers to the finger mechanism, three different modules were designed. These modules could be easily swapped to treat any of the finger joints. This was possible because each end effector blocked the motion of certain joints and enabled the rotation of one. As shown in Figure 2c, the MCP end effector was a cylinder covering the entire finger, allowing only MCP rotation. The PIP end effector included a ring to lock the MCP and a cylinder up to the PIP joint to lock the DIP. The DIP end effector had a cylinder blocking the MCP and PIP joints and a Velcro fingertip strap. To avoid mutual interference during full-finger joint actuation, a cable-driven system was implemented to allow coordinated movement across all joints by distributing force based on attachment points. The mechanical design ensures efficient force transmission, enabling smooth and self-regulating joint motion while minimizing interference between actuators. The system employs closed-loop feedback control using real-time finger angle measurements to dynamically adjust the SMA wire actuators. Additionally, an open-loop mode based on preset angle values is available for tasks where precise tracking is not essential. The kinematics analysis of the finger mechanism will be discussed in the next section.

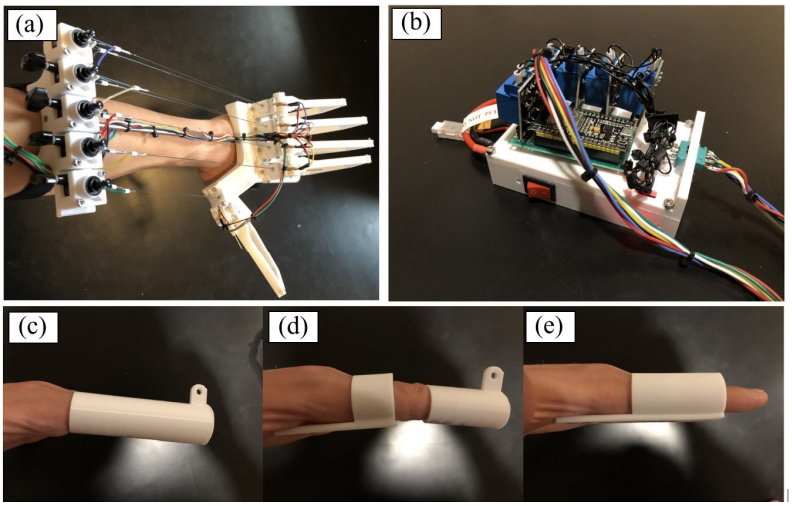

Figure 2. (**a**) Fabricated exoskeleton glove, (**b**) Control and power system, (**c**–**e**) Various end effectors designed for the treatment of the MCP, PIP, and DIP joints, respectively.

2.2. System Modeling and Control

The finger telerehabilitation exoskeleton is connected to the user's fingers via a series of joints and links, as illustrated in Figure 3a. This system consists of three links, which are interconnected by revolute joints, responsible for transmitting the input torque from the smart actuator to the user's finger. The patient's hand is securely fastened to the hand module using Velcro straps. Consequently, the user's hand and the hand module form a single, rigid link within the mechanism. This setup allows the finger-interaction portion of the exoskeleton to be modeled as a four-bar mechanism, where the user's hand and hand module serve as the reference or ground link. Due to this configuration, the system possesses a single degree of freedom. Figure 3b provides a generalized model of the finger-interaction mechanism. A uniform model can be used for all joints, with variations in lengths ($l_1 - l_4$) based on whether the MCP, PIP, or DIP joints are addressed. An offset

angle is also introduced for the PIP and DIP joints. To determine the displacement of the patient's finger joint, the angle θ_4 is modeled according to Equation (1).

$$\theta_4 = \pi - arcsin\frac{l_2}{\sqrt{l_1^2 + l_2^2 - 2l_1 l_2 cos\theta_2}} - arcsin\frac{l_3}{l_4}sin\alpha \tag{1}$$

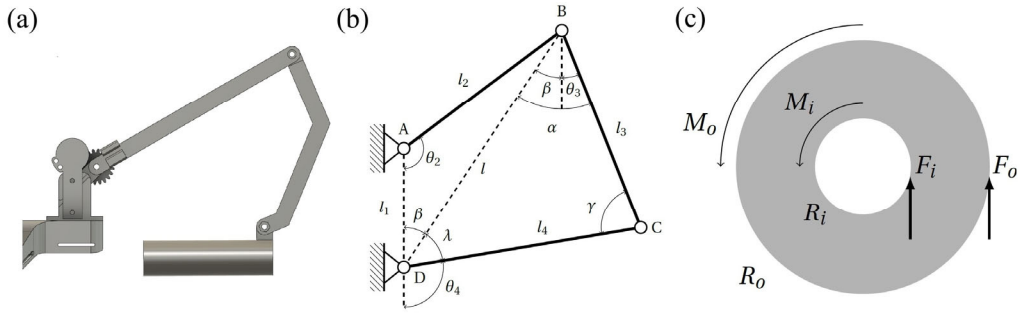

Figure 3. Linkage mechanism: (**a**) Side view, (**b**) Four-bar model, (**c**) Hollow disks friction model.

The kinematic analysis of the smart material exoskeleton system can be formulated using Equations (2)–(5). Here, k_i represents the known geometrical parameters related to length/angle, and $\theta_i^{\cdot}$ denotes angular velocity. As shown, the system can be fully characterized by the input angle θ_2.

$$\theta_4(\theta_2) = 2\arctan\left(-k_1 \pm \sqrt{k_1^2 + k_2^2 - k_3^2}, k_3 - k_2\right)^2 \tag{2}$$

$$\theta_3(\theta_2, \theta_4) = \arctan\left(-l_2 sin(\theta_2) + l_4 \sin(\theta_4), l_1 - l_2\cos(\theta_2) + l_4\cos(\theta_4)\right)^2 \tag{3}$$

$$\dot{\theta_3} = \frac{l_2 \sin(\theta_4 - \theta_2)}{l_3 \sin(\theta_3 - \theta_4)}\dot{\theta_2} \tag{4}$$

$$\dot{\theta_4} = \frac{l_2 \sin(\theta_3 - \theta_2)}{l_4 \sin(\theta_3 - \theta_4)}\dot{\theta_2} \tag{5}$$

After defining the kinematics framework, the dynamic equation of the system was determined using the Lagrangian formulation. This approach relies on the difference between the system's total kinetic energy T and total potential energy V. The complete dynamic equation of the hand mechanism is given in Equation (6). Detailed derivations of the parameters J_i, S_i, P_1, C_1, and G are provided in Appendix A.

$$\begin{aligned}\tau_{ext} = 2\left[J_1 + J_2 S_1^2 + J_3 S_2^2 + P_1 C_1 S_1\right]\ddot{\theta_2} + \Big[2J_2 S_1\left(\tfrac{\partial S_1}{\partial \theta_2} + S_1\tfrac{\partial S_1}{\partial \theta_3} + S_2\tfrac{\partial S_1}{\partial \theta_4}\right) + \\ 2J_3 S_2\left(\tfrac{\partial S_2}{\partial \theta_2} + S_1\tfrac{\partial S_2}{\partial \theta_3} + S_2\tfrac{\partial S_2}{\partial \theta_4}\right) + P_1\Big(C_1\left(\tfrac{\partial S_1}{\partial \theta_2} + S_1\tfrac{\partial S_1}{\partial \theta_3} + S_2\tfrac{\partial S_1}{\partial \theta_4}\right) + S_1\left(\tfrac{\partial C_1}{\partial \theta_2} + \\ S_1\tfrac{\partial C_1}{\partial \theta_3}\right)\Big)\Big]\dot{\theta_2} - \tfrac{\partial G}{\partial \theta_2} - S_1\tfrac{\partial G}{\partial \theta_3} - S_2\tfrac{\partial G}{\partial \theta_4}\end{aligned} \tag{6}$$

The external torque, denoted as τ_{ext}, consists of three main components: the restoring moment generated by the torsional spring, the moment caused by friction forces at the joint, and the torque produced by the smart material wire pulling the input arm. The restoring torque from the torsional spring depends on the spring's stiffness and angular displacement. Friction torque at the joint, modeled as the interaction of two rotating hollow disks (shown in Figure 3c), is detailed in Equation (7).

$$M_{fric} = -\frac{3}{4}\mu_k F_{load}\left(\frac{R_o^3 - R_i^3}{R_o^2 - R_i^2}\right) sgn\left(\dot{\theta_2}\right) \tag{7}$$

Here, μ_k is the coefficient of friction, and *Ri* and *Ro* are the inner and outer radii of the hollow disk, respectively. The net friction moment integrates the friction forces (F_o, F_i) over the disk's area, including a factor of two to account for the two contact areas between the input arm and the base.

The torque from the smart wire is calculated by multiplying the wire's pulling force by the vertical distance from the point of force application to the input arm's joint. To quantify the pulling force, a thermal model, a phase transformation model, and a mechanical model were used, as described in [38]. The smart actuator wire utilized in this study is made of a nickel-titanium alloy with shape memory properties, which activate upon reaching a specific temperature. To achieve the desired pulling force, an electrical current is applied to the wire, generating heat through its electrical resistance. This heating process, essential for the phase transformation from martensite to austenite, is modeled using Equation (8) [38].

$$C_W V_W \rho_W \frac{dT}{dt} = i^2 R - hA_w(T - T_a) \tag{8}$$

In this model, C_W denotes the specific heat of nickel-titanium, V_W is the wire's volume, ρ_W is the wire's density, T is the wire's temperature, i is the electrical current, R is the electrical resistance, h is the convection coefficient, A_w is the wire's surface area, and T_a is the surrounding ambient temperature. The pulling force of the SMW can be approximated by multiplying the cross-sectional area of the wire by the stress, derived from Hooke's law and strain. The strain in the SMW depends on the volume fraction of the phase transition and can be modeled as a conditional function ξ, according to Equation (9), which is based on A_s and A_f, the starting and finishing temperatures for the austenite transition.

$$\epsilon + \tau \frac{d\epsilon}{dt} = \epsilon_m(1 - \xi(T)) \tag{9}$$

where, ξ is the martensite fraction, τ is the mechanical time constant, ϵ is the mechanical strain, and ϵ_m is the maximum recoverable strain. The pulling force can be used to compute the moment created by the smart actuator, which is the main component of the external torque in the system modeling.

Once the system modeling is complete, the next step is to define the controller. Designing a model-based controller for shape memory alloys (SMAs) is challenging due to their nonlinear characteristics and hysteresis effects [39]. A viable alternative is to use variable structure controllers, which switch the control law discontinuously based on the system's state. A common and effective control strategy for SMAs is the bang-bang controller, which toggles between two states: fully active or completely inactive. Heating intensity and speed are modulated through Pulse Width Modulation (PWM), in line with the hardware design where relay switches control current flow through the SMA wire. One significant advantage of the bang-bang controller is its ability to drive the system rapidly to the desired position, as the relay remains engaged until the target is reached. This feature is particularly useful for SMAs, which typically have slow response times due to the heating and cooling processes. Additionally, friction at the joints helps reduce overshoot, making the bang-bang controller a practical option for this system. The controller and system model were integrated into a MATLAB Simulink simulation, as shown in Figure 4. This simulation was utilized to compare the theoretical angular displacement of the input link over time, given a desired angular position, with the experimentally observed angular displacement. Further details about the parameters used in the Simulink model can be found in Appendix B.

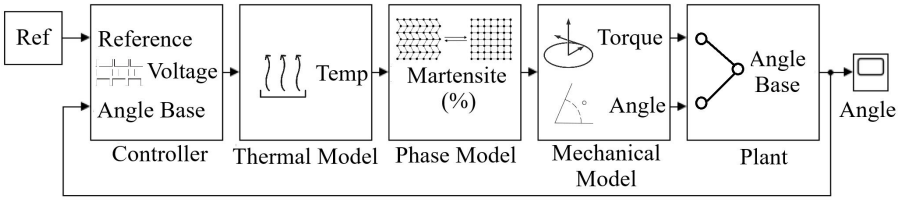

Figure 4. Schematic representation of the Simulink system model.

2.3. Numerical Modeling of Shape Memory Alloy

The phase transition behavior of the NiTi shape memory wire was investigated using COMSOL Multiphysics 6.2 software. The analysis employed the Souza–Auricchio model, which incorporates a transformation strain tensor derived from the limit function. The thermodynamic stress conjugated to the transformation strain is expressed in Equation (10) [40]. The transformation strain can be determined using the plastic multiplier λ_p as described in Equation (11).

$$\sigma_{tr} = dev(\sigma) - H_k \varepsilon_{tr} - \beta < T - T^* > \frac{\varepsilon_{tr}}{|\varepsilon_{tr}|} - \frac{\partial I}{\partial \varepsilon_{tr}} \tag{10}$$

$$\dot{\varepsilon_{tr}} = \lambda_p \frac{\partial \mathrm{F}}{\partial \sigma_{tr}} \tag{11}$$

where, T^* represents the reference temperature, H_k is the hardening modulus, and, β denotes the thermal coefficient. The term $dev(\sigma)$ indicates the deviatoric stress, representing the shear component of the stress. Additionally, I typically represents a state variable that accounts for the history and evolution of the material's phase transformation process. The hardening modulus H_k is derived from the difference between the martensite start and finish temperatures, as described in Equation (12).

$$H_k = \frac{C_M\left(M_s - M_f\right)}{\varepsilon_{tr,max}} = \frac{\sigma_{Mf} - \sigma_{Ms}}{\varepsilon_{tr,max}} \tag{12}$$

During the modeling procedure, it is assumed that the slope of the limit curves in both the martensite and austenite domains are equal. Furthermore, the widths of the transition zones are also assumed to be equal. This implies that the temperature difference between the austenite finish temperature (A_f) and austenite start temperature (A_s) is equal to the temperature difference between the martensite start temperature (M_s) and martensite finish temperature (M_f). The material properties related to the phase change are detailed in Appendix C.

2.4. Remote Control System

The proposed Human–Machine Interface (HMI) system combines hardware and software to enable remote control and monitoring of a glove-based finger telerehabilitation exoskeleton. The system uses an ESP-32 microcontroller (Arduino, Torino, Italy) programmed in C++ with the Real-Time Operating System (RTOS) library to handle two tasks. The first task sets up a web server hosting an HTML interface for exoskeleton control, managed by a Web Server Wrapper for network settings and operations. This interface features sliders for each finger, allowing real-time monitoring and adjustment of patient progress. Slider updates are sent via WebSocket to the server, which broadcasts the data to all clients for synchronization. The second task runs the control algorithm, using DigitalOut and Relay objects for relay states and potentiometers for precise finger position measurement, thus controlling the glove's actuators. An Arduino microcontroller (Arduino, Italy) adjusts the relay's duty cycle based on slider values, enhancing user interaction with real-time feedback and control. The integration of WebSocket technology ensures low-latency communication, making the system responsive and reliable for telerehabilitation. The front panel of the HMI is illustrated in Figure 5. It should be noted that rehabilitation systems

with slow, controlled movements allow for higher delay tolerance in remote control. Tests show delays of under 150 ms, even in unstable network conditions, which is well below the 200 ms acceptable limit. Since rehabilitation movements take several seconds, delays of up to 200 ms do not interfere with therapeutic goals.

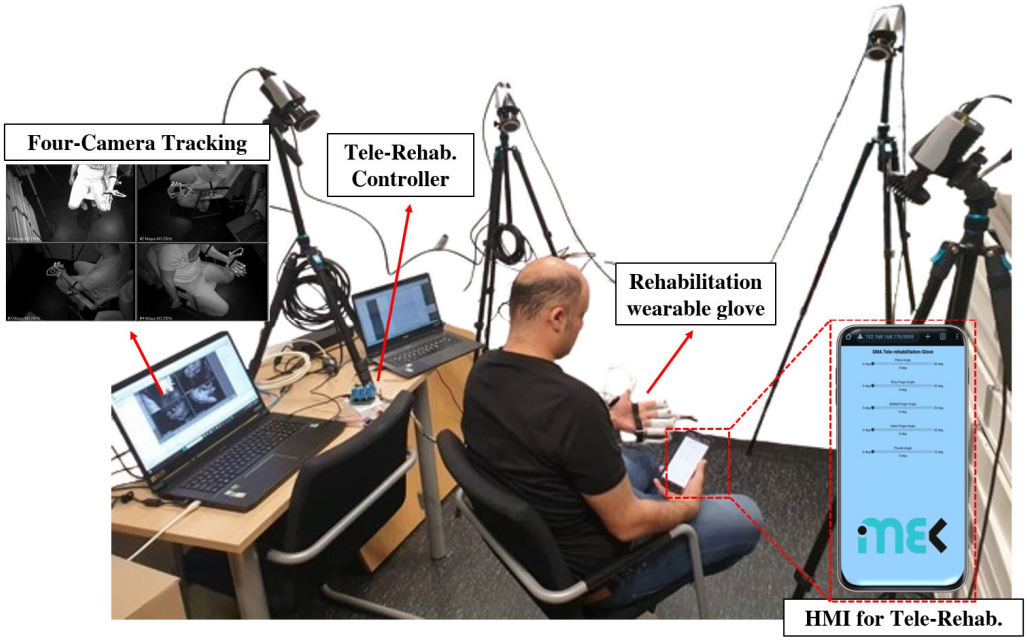

Figure 5. Measurement apparatus for evaluating dynamic finger movements.

2.5. Measurement Scheme

2.5.1. Dynamic Measurement

To record the joint angular displacement, data from the potentiometer were analyzed, corresponding to the input link's displacement. This data was then converted to the actual joint displacement based on the kinematic analysis discussed in Section 2.2. This was possible because the four-bar mechanism is a one-degree-of-freedom system. To analyze the produced torque at the joints, force measurements were conducted using a force sensor (FSR402, Interlink Electronics, Irvine, CA, USA) over a period of 7 s. The amplified signal was sent to a microcontroller under the full activation mode of the SMW. The force values obtained were then multiplied by the lever arm distance to calculate the torque. The finger moving distance was measured with the camera tracking system (Qualisys—Miqus M5, Qualisys, Göteborg, Sweden). The tracking system was calibrated using Qualisys Track Manager 2022.2 (QTM) software and a standard fiber carbon L-frame. The maximum average error for all axes was 0.235 mm, which is within the acceptable range for rehabilitation purposes. The capture rate was set at 100 Hz, and the sensor resolution was configured to 2 MP at 340 Hz. It should be noted that the accuracy of the distance-traveled calculation depends on the sampling frequency and the speed of the trajectory marker. To mitigate noise accumulation in the results, a hysteresis of 0.2 mm is applied in the software, reducing noise during the stationary segments of the trajectory. The measurement setup is illustrated in Figure 5.

2.5.2. Static Measurement

To assess the level of force a user can apply when manipulating different cylindrical objects, a lightweight handmade Sensor Grip was developed. Figure 6 illustrates the schematic of the fabricated sensor and calibration curve. The Grip contains three internal FSR-FX29 sensors (TE Connectivity, Schaffhausen, Switzerland), allowing force measurement across three different surface areas. The electrical signal from each sensor was processed via Arduino based on the calibration value. Calibration of the FX29 was conducted using

weight blocks. After calibration, a linear regression fit was applied to the measured data points, resulting in an R^2 value above 0.956% for a force range between 1 and 10 N. It is noteworthy that the linearity error and repeatability of the sensor were within ±0.01% and ±0.8%, respectively.

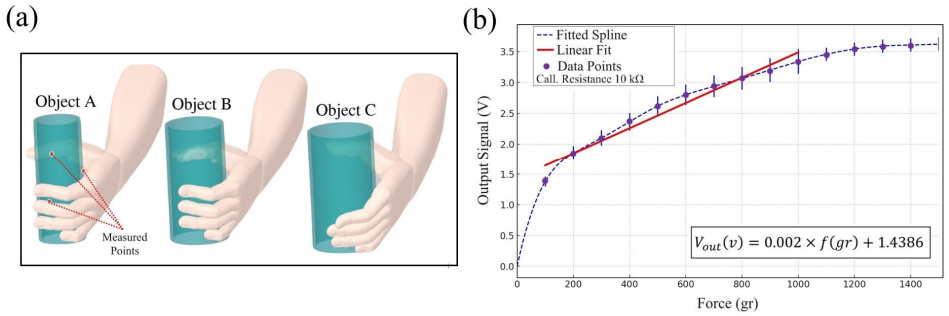

Figure 6. (**a**) Schematic depiction of the Grip Sensor and test objects, (**b**) Calibration results.

3. Results and Discussion

To evaluate the developed model against the actual behavior of the exoskeleton, an experimental verification test was conducted. In this experiment, the reference path involved moving to 20°, holding that position for 20 s, then moving to 30° and holding for another 20 s, and finally returning to the initial position. The displacements referred to changes in the θ_2 variable as discussed in Section 2.2. As illustrated in Figure 7, the Simulink result closely matched the observed behavior during the trials. Both curves commenced motion at approximately 1.5 s, corresponding to the time required for the formation of initial austenite structures and the resulting pulling force. Furthermore, both curves reached the first reference point of 20° around 2.5 s. Overshooting was observed in both curves, with a magnitude reaching up to 5° during the trials. This overshooting was attributed to the wire's temperature exceeding the full austenite temperature upon reaching the desired position, causing the SMA wire to continue exerting pulling forces until the temperature dropped below the full austenite threshold. Upon reaching the desired reference after overshooting, the position continued to decrease for the same reason. It took additional time for the wire to reach the full austenite temperature again and exert the same level of pulling forces. The model exhibited a greater degree of undershooting due to the manner in which the stress–strain relationship of the alloy was modeled. In the Simulink model, a linear relationship was used, generating insufficient forces during the initial transitions to austenite. During the second path change to 30°, less overshooting was observed because the torsional spring exerted greater returning forces at that position. Finally, the angular displacements during the cooldown phase were slower, as observed in both the trials and the model. The overall average angular displacement error was calculated to be 2.76°, which was considered acceptable.

The phase transition behavior of the shape memory wire was investigated through numerical modeling. Figure 8a illustrates that the applied DC current resulted in a linear increase in von Mises stress with temperature. This linearity was expected due to the uniform heating effect of the steady current. The color gradient, representing the martensite volume fraction, transitioned smoothly from blue to yellow as temperature rose, indicating a gradual phase transformation. However, as shown in Figure 8b, the effects of PWM stimulation revealed a more complex and nonlinear stress response. The abrupt changes in the color gradient implied dynamic phase transformations, suggesting reduced stability in the phase change process. PWM's rapid switching may have introduced fluctuations, contributing to more complex hysteresis behavior. Despite this, the nonlinear stress response indicated a faster phase transformation at lower temperatures. While PWM might increase movement speed, the complexity of its nonlinear behavior and the added hysteresis necessitated further investigation to determine the optimal parameters.

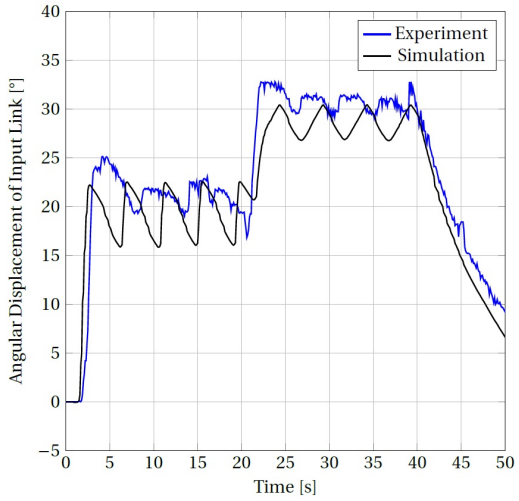

Figure 7. Comparison of simulation and experimental test for a profile input.

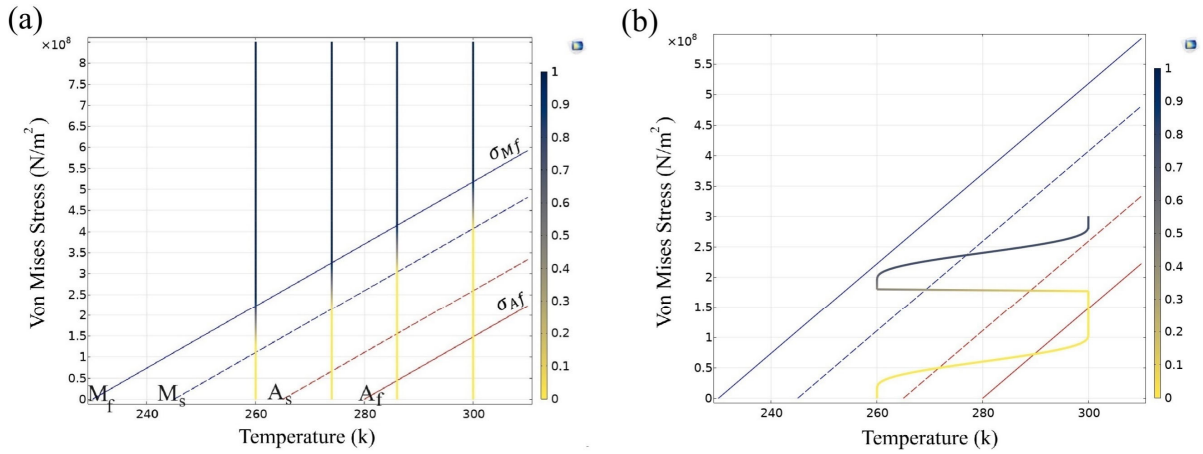

Figure 8. Stress–temperature phase diagrams for NiTi shape memory alloy wire: (**a**) Under different constant DC voltage stimulation, (**b**) Under PWM stimulation signals. The color legend indicates the martensite volume fraction.

Figure 9 illustrates the distance traveled by the index finger during rehabilitation at two different speeds, highlighting the impact of varying PWM levels. It is evident from the figure that applying a higher PWM to the SMA actuator enhances performance and reduces velocity variations. Higher PWM levels seem to promote efficient phase transitions, allowing the SMA to fully transform from the martensitic to the austenitic phase. As a result, the shape memory effect is strengthened, providing better control and stability of movements. Operating consistently within the optimal phase transition range minimizes hysteresis and irregularities, which is essential for precise and predictable movements in rehabilitation applications.

The performance of the rehabilitation system for gripping tasks was experimentally investigated using a homemade handle designed in cylindrical shapes with varying diameters. The results are detailed in Table 1. The reported values for each sensor are the averages of repeated measurements to minimize potential errors. The gripping forces were recorded on three sides of the handle sensor. It was observed that Sensor 2, positioned on the mid-hand side of the handle, registered the lowest force. The high standard deviation in measurements was due to improper surface contact with the hand, a consequence of the constraints in the exoskeleton design. Despite this limitation, the average measured force was 7.64 N, which is considered adequate for everyday gripping activities and aligns with findings from previous research in the literature [41,42]. The grip force tests confirmed

that the finger rehabilitation robot effectively assists in grasping cylinders with diameters between 60 mm and 80 mm.

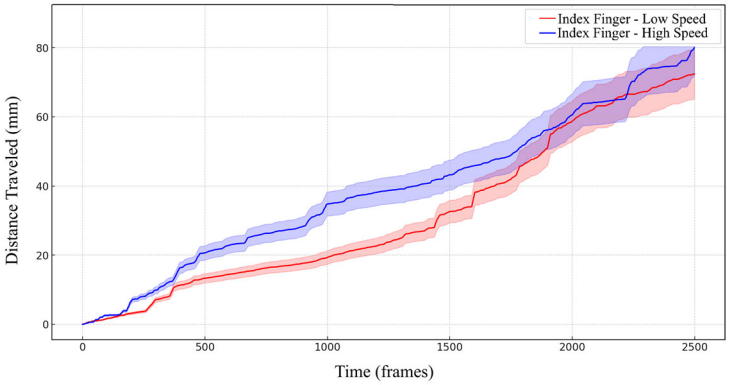

Figure 9. Experimental results of finger movement measurements at different input speeds, with transparent margins indicating the measurement error bands.

Table 1. Force evaluation with handle sensor for gripping activities.

Parameter (Diameter)	Sensor 1 (N)	Sensor 2 (N)	Sensor 3 (N)	Total Force (N)
Object A (60 mm)	2.96 ± 1.02	1.12 ± 0.92	2.45 ± 1.52	6.53
Object B (70 mm)	3.27 ± 1.27	1.17 ± 1.04	2.87 ± 0.92	7.31
Object C (80 mm)	4.13 ± 0.85	1.43 ± 1.15	3.53 ± 1.23	9.09

Further evaluation of the exo-glove was conducted through experimental measurements of the angular displacement and torque for each joint: MCP, PIP, DIP, and IP. The protocol set a reference path for all fingers, excluding the thumb, to an initial position of 30°, adjusted to zero at the 20-s mark. For the thumb, the reference path was set to 10° due to its smaller range of motion in the MCP joint. Figure 10a–c illustrate the measurement results for angular displacement and torque of each joint. Figure 10a shows that all fingers, except the thumb, achieved a range of motion close to 30° at the MCP joint. The thumb reached 25° and remained there a few seconds after the 20-s mark, attributed to increased friction at the base module. The thumb's angular position stabilized around 10° due to low initial tension in the torsional spring and excessive friction. Variations in final angular positions among fingers can be explained by differences in finger sizes, joint locations, and torsional springs' characteristics. For the PIP joint, the MCP and DIP joints were immobilized for all fingers. Figure 10b indicates that angular displacements at the PIP joint were greater than those at the MCP joint due to the reduced lever arm from the force application point. The ring finger exhibited the highest displacement at 80°, while the index finger had the lowest at 70°, highlighting the benefit of a reduced lever arm for finger rehabilitation. In the DIP joint assessment, with the MCP and PIP joints immobilized, large angular displacements were observed due to the proximity to the fingertips. Figure 10c shows substantial displacements for the DIP and IP joints, with the ring, middle, index, and pinkie fingers exhibiting displacements ranging from 60° to 70°.

It should be noted that although frictional forces at the thumb's MCP joint were observed to increase slightly, this variation does not significantly impact the device's performance in delivering controlled, repeatable rehabilitation exercises. The system's design, including its SMA actuators and torsional springs, effectively compensates for any minor frictional resistance, ensuring that the device remains functional and reliable for its primary rehabilitative purpose.

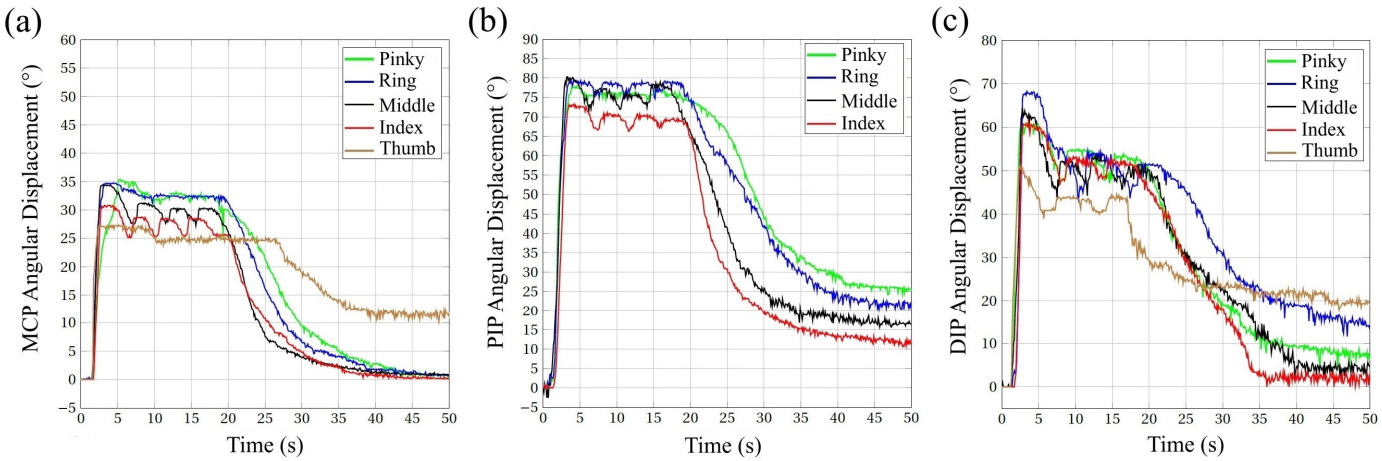

Figure 10. Experimental results of the joint displacements for all fingers: (**a**) Metacarpophalangeal (MCP) joint, (**b**) Proximal Interphalangeal (PIP) joint, and (**c**) Distal Interphalangeal/Interphalangeal (DIP/IP) joint.

Figure 11a illustrates that torque at the MCP joint varied for each finger based on its dimensions, directly influencing the lever arm. The middle finger exhibited the highest torque at approximately 0.8 Nm, while the thumb's MCP joint had the lowest at 0.3 Nm. In Figure 11b, torques at the PIP joint were lower than those at the MCP joint due to the shorter distance between the force application point and the joint. The middle finger's PIP joint produced a maximum torque of 0.4 Nm, whereas the pinky finger's PIP joint had the lowest torque at 0.2 Nm. A similar trend was observed in Figure 11c for the torques at the DIP and IP joints. The middle finger achieved a torque greater than 0.2 Nm, while the pinky finger exhibited a torque of approximately 0.1 Nm.

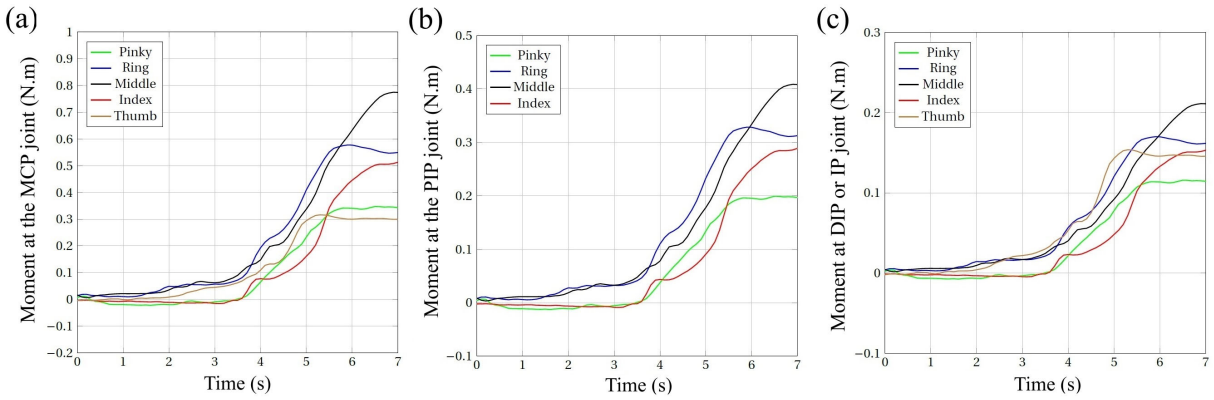

Figure 11. Experimental results of the torque measurement for all fingers: (**a**) Metacarpophalangeal (MCP) joint; (**b**) Proximal Interphalangeal (PIP) joint, and (**c**) Distal Interphalangeal/Interphalangeal (DIP/IP) joint.

The experimental data demonstrate that the exoskeleton glove generates sufficient torque across all fingers and joints, enabling successful movement to the desired positions during rehabilitation sessions. This capability underscores the glove's effectiveness in providing targeted therapeutic interventions.

4. Conclusions

This research successfully developed and tested a lightweight, wearable exo-glove specifically designed for finger telerehabilitation using NiTi shape memory alloy (SMA) actuators. The exo-glove effectively controls the metacarpophalangeal (MCP), proximal interphalangeal (PIP), and distal interphalangeal (DIP) joints. The integration of a variable structure controller, managed through a web-based Human–Machine Interface (HMI),

enables precise remote adjustments, significantly enhancing the device's versatility in telerehabilitation. Thermal behavior and phase change dynamics of the SMA actuators were modeled using MATLAB Simulink. Furthermore, the phase transformation characteristics of the NiTi SMA wires were analyzed with the Souza–Auricchio model in COMSOL Multiphysics 6.2 software. Verification tests confirmed the accuracy of the Simulink model, with an average error of 2.76°. Simulation results revealed that, while DC current application resulted in a linear increase in von Mises stress with temperature, PWM stimulation induced a more complex, nonlinear stress response accompanied by dynamic phase transformations. These findings underscore the need for further investigation to optimize operational parameters. Experimental results demonstrated a range of motion for the MCP, PIP, and DIP joints of 21°, 65°, and 60.3°, respectively. Additionally, a minimum torque of 0.2 Nm at each finger joint was achieved, sufficient to counteract joint resistance and meet rehabilitation torque requirements. These outcomes affirm the exo-glove's capability to provide the necessary torque and motion for effective remote rehabilitation, potentially enhancing patient outcomes by reducing dependence on in-person therapy sessions.

In real-world rehabilitation scenarios, the degree of error observed in this study was not critical, and the system remains capable of delivering the intended rehabilitation exercises. However, refining the control mechanisms to enhance precision, prevent degradation, and reduce the hysteresis effect can be achieved through the use of a feedforward control method or by fine-tuning the PWM stimulation signal. Both of these approaches present potential avenues for future research. Furthermore, additional investigation is required to optimize the balance between functionality, comfort, speed, and long-term durability of the exo-glove, highlighting key areas for continued development.

Author Contributions: Conceptualization, A.A.; methodology, J.P.K.B. and AA.; software, M.S., J.P.K.B. and A.A.; investigation, M.S., A.A., J.P.K.B. and T.A.K.; formal analysis, J.P.K.B., A.A. and M.S.; supervision, T.A.K.; validation, A.A. and T.A.K.; project administration, A.A.; funding acquisition, T.A.K.; writing—original draft preparation, M.S.; writing—review and editing, M.S., A.A. and T.A.K. All authors have read and agreed to the published version of the manuscript.

Funding: Publishing fees were supported by the Funding Program Open Access Publishing of Hamburg University of Technology (TUHH).

Informed Consent Statement: Not applicable.

Data Availability Statement: The data that support the findings of this study are available from the corresponding author upon request.

Conflicts of Interest: The authors declare no conflict of interest.

Appendix A

$$S_1(\theta_2, \theta_3, \theta_4) = \frac{l_2 \sin(\theta_4 - \theta_2)}{l_3 \sin(\theta_3 - \theta_4)} \tag{A1}$$

$$S_2(\theta_2, \theta_3, \theta_4) = \frac{l_2 \sin(\theta_3 - \theta_2)}{l_4 \sin(\theta_3 - \theta_4)} \tag{A2}$$

$$J_1 = \frac{1}{2}(m_2 l_{c2}^2 + I_2 + m_3 l_2^2) \tag{A3}$$

$$J_2 = \frac{1}{2}(m_3 l_{c3}^2 + I_3) \tag{A4}$$

$$J_3 = \frac{1}{2}(m_4 l_{c4}^2 + I_4) \tag{A5}$$

$$P_1 = m_3 l_2 l_{c3} \tag{A6}$$

$$C_1 = \cos(\theta_2 - \theta_3) \tag{A7}$$

$$G = (-m_2 g l_{c2} - m_3 g l_2) sin\theta_2 - m_3 g l_{c3} sin\theta_3 - m_4 g l_{c4} sin\theta_4 \tag{A8}$$

Appendix B

Table A1. Parameters and values used in the Simulink model.

Description	Symbol	Value (Unit)
Length of link 1	l_1	0.05 (m)
Length of link 2	l_2	0.14 (m)
Length of link 3	l_3	0.08 (m)
Length of link 4	l_4	0.11 (m)
Initial link 2 angle	$\theta_2(0)$	$2\pi/3$ (rad)
Mass of link 2	m_2	0.01 (kg)
Mass of link 3	m_3	0.007 (kg)
Mass of link 4	m_4	0.1 (kg)
Stiffness of torsional spring	k_s	0.804 ($\mathrm{Nm \cdot rad^{-1}}$)
PLA coefficient of friction	μ_k	0.45 ($\mathrm{NN^{-1}}$)
Clamping force on the link 2 joint	F_{load}	15 (N)
Inner diameter of friction hollow disk	R_i	1.8×10^{-2} (m)
Outer diameter of friction hollow disk	R_o	5×10^{-3} (m)
Length of the SMA wire	l	0.67 (m)
Electrical resistance of the SMA wire	R	5.56 (Ω)

Appendix C

Table A2. Material properties of phase change.

Material Parameter	Symbol	Value (Unit)
Maximum transformation strain	$\varepsilon_{tr,max}$	0.056 (1)
Slope of limit curve	β	7.4 (MPa/k)
Reference temperature	T^*	265.5 K
Elastic domain radius	σ_o	129.5 MPa
Hardening modulus	H_k	1.982 GPa

References

1. Benjamin, E.J.; Blaha, M.J.; Chiuve, S.E.; Cushman, M.; Das, S.R.; Deo, R.; de Ferranti, S.D.; Floyd, J.; Fornage, M.; Gillespie, C.; et al. Heart disease and stroke statistics-2017 update: A report from the American Heart Association. *Circulation* **2017**, *135*, e146–e603. [CrossRef] [PubMed]
2. Knecht, S.; Hesse, S.; Oster, P. Rehabilitation after stroke. *Dtsch. Arztebl. Int.* **2011**, *108*, 600–606. [CrossRef] [PubMed]
3. Mackay, J.; Mensah, G. *Atlas of Heart Disease and Stroke*; World Health Organization, Nonserial Publication: Brighton, UK, 2004.
4. Parker, V.M.; Wade, D.T.; Langton, H.R. Loss of arm function after stroke: Measurement, frequency, and recovery. *Int. Rehabil. Med.* **1986**, *8*, 69–73. [CrossRef] [PubMed]
5. Marty, J.; Porcher, B.; Autissier, R. Hand injuries and occupational accidents. Statistics and prevention. *Ann. Chir. Main.* **1983**, *2*, 368–370. [CrossRef]
6. van Stormbroek, K.; Buchanan, H. Novice therapists in a developing context: Extending the reach of hand rehabilitation. *Hand Ther.* **2017**, *22*, 141–152. [CrossRef]
7. Lingampally, P.K.; Ramanathan, K.C.; Shanmugam, R.; Cepova, L.; Salunkhe, S. Wearable Assistive Rehabilitation Robotic Devices—A Comprehensive Review. *Machines* **2024**, *12*, 415. [CrossRef]
8. Li, F.; Chen, J.; Ye, G.; Dong, S.; Gao, Z.; Zhou, Y. Soft robotic glove with sensing and force feedback for rehabilitation in virtual reality. *Biomimetics* **2023**, *8*, 83. [CrossRef]
9. Janarthanan, V.; Assad-Uz-Zaman, M.; Rahman, M.H.; McGonigle, E.; Wang, I. Design and development of a sensored glove for home-based rehabilitation. *J. Hand Ther.* **2020**, *33*, 209–219. [CrossRef]
10. Aly, A.A.I.; Abbasimoshaei, A.; Kern, T.A. Developing a VR training environment for fingers rehabilitation. In Proceedings of the 13th International Conference on Human Haptic Sensing and Touch Enabled Computer Applications, EuroHaptics 2022, Hamburg, Germany, 22–25 May 2022; pp. 331–333.

11. Haghshenas-Jaryani, M.; Pande, C.; Wijesundara, B.M. Soft robotic bilateral hand rehabilitation system for fine motor learning. In Proceedings of the 2019 IEEE 16th International Conference on Rehabilitation Robotics (ICORR), Toronto, ON, Canada, 24–28 June 2019; pp. 337–342.
12. Yang, S.-H.; Koh, C.-L.; Hsu, C.-H.; Chen, P.-C.; Chen, J.-W.; Lan, Y.-H.; Yang, Y.; Lin, Y.-D.; Wu, C.-H.; Liu, H.-K.; et al. An instrumented glove-controlled portable hand-exoskeleton for bilateral hand rehabilitation. *Biosensors* **2021**, *11*, 495. [CrossRef]
13. Cisnal, A.; Gordaliza, P.; Pérez Turiel, J.; Fraile, J.C. Interaction with a hand rehabilitation exoskeleton in EMG-driven bilateral therapy: Influence of visual biofeedback on the users' performance. *Sensors* **2023**, *23*, 2048. [CrossRef]
14. Connolly, J.; Condell, J.; O'Flynn, B.; Sanchez, J.T.; Gardiner, P. IMU sensor-based electronic goniometric glove for clinical finger. movement analysis. *IEEE Sens. J.* **2017**, *18*, 1273–1281. [CrossRef]
15. Lin, B.S.; Lee, I.J.; Yang, S.Y.; Lo, Y.C.; Lee, J.; Chen, J.L. Design of an inertial-sensor-based data glove for hand function evaluation. *Sensors* **2018**, *18*, 1545. [CrossRef] [PubMed]
16. Saggio, G.; Riillo, F.; Sbernini, L.; Quitadamo, L.R. Resistive flex sensors: A survey. *Smart Mater. Struct.* **2015**, *25*, 013001. [CrossRef]
17. Guo, S.; Gao, J.; Guo, J.; Zhang, W.; Hu, Y. Design of the structural optimization for the upper limb rehabilitation robot. In Proceedings of the 2016 IEEE International Conference on Mechatronics and Automation, Harbin, China, 7–10 August 2016; pp. 1185–1190.
18. Richards, C.; MacKenzie, N.; Roberts, S.; Escorpizo, R. People with spinal cord injury in the United States. *Am. J. Phys. Med. Rehabil.* **2017**, *96*, S124–S126. [CrossRef] [PubMed]
19. Popov, D.; Gaponov, I.; Ryu, J.H. Portable exoskeleton glove with soft structure for hand assistance in activities of daily living. *IEEE ASME Trans. Mechatron.* **2017**, *22*, 865–875. [CrossRef]
20. Lee, B.J.; Williams, A.; Ben-Tzvi, P. Intelligent object grasping with sensor fusion for rehabilitation and assistive applications. *IEEE Trans. Neural Syst. Rehabil. Eng.* **2018**, *26*, 1556–1565. [CrossRef]
21. Chen, X.; Gong, L.; Wei, L.; Yeh, S.-C.; Da Xu, L.; Zheng, L.; Zou, Z. A wearable hand rehabilitation system with soft gloves. *IEEE Trans. Ind. Inform.* **2021**, *17*, 943–952. [CrossRef]
22. Lai, J.; Song, A.; Shi, K.; Ji, Q.; Lu, Y.; Li, H. Design and evaluation of a bidirectional soft glove for hand rehabilitation-assistance tasks. *IEEE Trans. Med. Robot. Bionics* **2023**, *3*, 730–740. [CrossRef]
23. Schabowsky, C.N.; Godfrey, S.B.; Holley, R.J.; Lum, P.S. Development and pilot testing of HEXORR: Hand EXOskeleton rehabilitation robot. *J. NeuroEng. Rehabil.* **2010**, *7*, 36. [CrossRef]
24. Shian, S.; Bertoldi, K.; Clarke, D.R. Dielectric elastomer based grippers for soft robotics. *Adv. Mater.* **2015**, *27*, 6814–6819. [CrossRef]
25. Xiloyannis, M.; Cappello, L.; Khanh, D.B.; Yen, S.-C.; Masia, L. Modelling and design of a synergy-based actuator for a tendon-driven soft robotic glove. In Proceedings of the 6th IEEE International Conference on Biomedical Robotics and Biomechatronics, Singapore, 26–29 June 2016; pp. 1213–1219.
26. Haptx. Available online: https://haptx.com/ (accessed on 2 July 2021).
27. Wang, J.; Fei, Y.; Pang, W. Design, modeling, and testing of a soft pneumatic glove with segmented pneuNets bending actuators. *IEEE ASME Trans. Mechatron.* **2019**, *24*, 990–1001. [CrossRef]
28. Feng, M.; Yang, D.; Gu, G. High-force fabric-based pneumatic actuators with asymmetric chambers and interference-reinforced structure for soft wearable assistive gloves. *IEEE Robot. Autom. Lett.* **2021**, *6*, 3105–3111. [CrossRef]
29. Yi, J.; Chen, X.; Wang, Z. A three-dimensional-printed soft robotic glove with enhanced ergonomics and force capability. *IEEE Robot. Autom.* **2018**, *3*, 242–248. [CrossRef]
30. Ge, L.; Chen, F.; Wang, D.; Zhang, Y.; Han, D.; Wang, T.; Gu, G. Design, modeling, and evaluation of fabric-based pneumatic actuators for soft wearable assistive gloves. *Soft Robot.* **2020**, *7*, 583–596. [CrossRef] [PubMed]
31. Kubášová, K.; Drátovská, V.; Losertová, M.; Salvetr, P.; Kopelent, M.; Kořínek, F.; Havlas, V.; Džugan, J.; Daniel, M. A Review on Additive Manufacturing Methods for NiTi Shape Memory Alloy Production. *Materials* **2024**, *17*, 1248. [CrossRef] [PubMed]
32. Chujo, T.; Sawada, H. The application of micro-vibratory phenomena of a shape-memory alloy wire to a novel vibrator. *Vibration* **2023**, *6*, 584–598. [CrossRef]
33. Grigorie, T.L.; Botez, R.M. A self–tuning intelligent controller for a smart actuation mechanism of a morphing wing based on shape memory alloys. *Actuators* **2023**, *12*, 350. [CrossRef]
34. Zhang, H.; Zhao, L.; Li, A.; Xu, S. Design and Hysteretic Performance Analysis of a Novel Multi-Layer Self-Centering Damper with Shape Memory Alloy. *Buildings* **2024**, *14*, 483. [CrossRef]
35. Wang, Y.; Zheng, S.; Pang, J.; Li, S.; Li, J. Design and experiment of a hand movement device driven by shape memory alloy wires. *J. Robot.* **2021**, *2021*, 6611581. [CrossRef]
36. Terrile, S.; Miguelañez, J.; Barrientos, A. A soft haptic glove actuated with shape memory alloy and flexible stretch sensors. *Sensors* **2021**, *21*, 5278. [CrossRef]
37. Lee, S.M.; Park, J. A soft wearable exoglove for rehabilitation assistance: A novel application of knitted shape-memory alloy as a flexible actuator. *Fash. Text.* **2024**, *11*, 14. [CrossRef]
38. Abdelaal, W.G.A.; Nagib, G. Modeling and simulation of sma actuator wire. In Proceedings of the 2014 9th International Conference on Computer Engineering & Systems (ICCES), Cairo, Egypt, 22–23 December 2014; pp. 401–405.

39. Kazeminasab, S.; Hadi, A.; Alipour, K.; Elahinia, M. Force and motion control of a tendon-driven hand exoskeleton actuated by shape memory alloys. *Ind. Robot. Int. J.* **2018**, *45*, 623–633. [CrossRef]
40. Auricchio, F.; Petrini, L. A three-dimensional model describing stress temperature induced solid phase transformations: Solution algorithm and boundary value problems. *Int. J. Numer. Methods Eng.* **2004**, *61*, 807–836. [CrossRef]
41. Saharan, L.; de Andrade, M.J.; Saleem, W.; Baughman, R.H.; Tadesse, Y. iGrab: Hand orthosis powered by twisted and coiled polymer muscles. *Smart Mater. Struct.* **2017**, *26*, 105048. [CrossRef]
42. Duanmu, D.; Li, X.; Huang, W.; Hu, Y. Soft Finger Rehabilitation Exoskeleton of Biomimetic Dragonfly Abdominal Ventral Muscles: Center Tendon Pneumatic Bellows Actuator. *Biomimetics* **2023**, *8*, 614. [CrossRef]